Journal of Power Sources 670 (2026) 239536

Contents lists available at ScienceDirect

Journal of Power Sources

journal homepage: www.elsevier.com/locate/jpowsour

Crystal chemistry and interface stability of ceria and doped $SrFeO_3$ with reduced critical raw materials

Costanza Tedesco [a], Marta Ippolito [a], Marine Cotte [b,c,d], Sebastian Vecino-Mantilla [e], Fabiana Matos de Oliveira [e], Massimiliano Lo Faro [e], Francesco Giannici [a,*]

[a] Department of Physics and Chemistry, University of Palermo, Viale delle Scienze, 90128, Palermo, Italy
[b] European Synchrotron Radiation Facility, 71 av des Martyrs, 38000, Grenoble, France
[c] France and Sorbonne Université, CNRS UMR 8220, LAMS, 4 pl. Jussieu, cedex 05, 75252, Paris, France
[d] Laboratoire d'Archeologie Moleculaire et Structurale, CNRS UMR 8220, Sorbonne Université, UPMC Univ Paris 06, Place Jussieu 4, 75005, Paris, France
[e] Institute of Advanced Energy Technologies (ITAE) of the Italian National Research Council (CNR), Via Salita S. Lucia sopra Contesse 5, 98126, Messina, Italy

HIGHLIGHTS

- Sr-segregation suppression in doped SrFeO3 electrode for reversible IT-SOCs.
- Synchrotron micro-XRF maps after electrochemical polarization.
- Micro-XANES probes redox states.
- Local FeO_6 distortion and oxygen-vacancy formation correlate with ionic transport.

ARTICLE INFO

Keywords:
X-ray microspectroscopy
SOFC
SOEC
Cathodes
Ceria

ABSTRACT

X-ray microspectroscopy provides a powerful insight into the chemical and structural evolution of complex materials under operating conditions, providing a spatially resolved analysis of interfaces and redox processes in solid-state devices. In this work, synchrotron-based micro X-ray fluorescence (micro-XRF) and micro X-ray absorption near-edge structure (micro-XANES) at the Fe K-edge were combined to investigate $SrFeO_3$-based perovskites co-doped with Ca, Ba, and Mo (SBCFM, SBC10FM) as well as $CaFeO_3$-based perovskites co-doped with Sr, Ba, and Mo (CBSFM) as electrode materials for reversible intermediate-temperature solid oxide electrochemical cells (IT-SOCs). These techniques allowed detailed mapping of elemental distributions, oxidation states, and interfacial features after electrochemical polarization. Overpotential measurements revealed that SBC10FM exhibits the best performance and structural stability at 700–800 °C, while CBSFM, despite its biphasic nature, shows the lowest activation energy for oxygen ion migration (0.47 eV) and high conductivity at lower temperatures. Micro-XRF maps identified a dense interfacial layer enriched in Ca, Ba, and Fe for SBCFM, whereas SBC10FM showed no densification and only limited Ca migration. Notably, Sr segregation, typically a major degradation mechanism in Sr-based electrodes, was completely suppressed in all samples, confirming the stabilizing role of multi-doping. Micro-XANES spectra demonstrated that Fe maintained a stable mixed-valence state (+3/+4) and coordination geometry throughout the electrode and interface, indicating strong redox resilience. The enhanced pre-edge intensity suggested distortion of FeO_6 octahedra and formation of oxygen vacancies, both linked to improved electrocatalytic activity. Altogether, the combined micro-XRF/micro-XANES approach elucidates local chemical mechanisms governing phase stability and performance, guiding the rational design of durable, resource-efficient electrodes for next-generation solid oxide electrochemical cells-based technologies.

* Corresponding author.
E-mail address: francesco.giannici@unipa.it (F. Giannici).

https://doi.org/10.1016/j.jpowsour.2026.239536
Received 5 December 2025; Received in revised form 21 January 2026; Accepted 1 February 2026
Available online 5 February 2026

1. Introduction

The continuous advancement in the field of materials for energy relies heavily on characterization techniques that can unveil chemical, structural, and functional complexities at the microscale. In this context, synchrotron-based X-ray microspectroscopy methods, such as micro X-Ray Fluorescence (micro-XRF) and micro X-Ray Absorption Near-Edge Structure (micro-XANES) have emerged as powerful and increasingly useful tools to investigate heterogeneous solid-state systems also under *in situ* conditions [1,2]. These techniques enable spatially resolved characterization of elemental distributions and chemical states with submicrometric resolution, providing insights that complement bulk methods whenever interface and surface effects are of interest. X-ray microanalyses have long been established as valuable tools in a wide range of fields such as life and earth science, but also in conservation of cultural heritage, where they are routinely used to investigate the elemental composition and chemical state of pigments, ceramics, metals, and other ancient artifacts in a non-destructive manner [2–4]. The ability to combine high spatial resolution, chemical sensitivity, and minimal sample preparation has made them particularly attractive for analysing heterogeneous materials, composites and interfaces [3,4]. More recently, these capabilities have attracted interest in the field of energy materials, where similar challenges of complexity, heterogeneity, and the need for *in situ*, *operando* or *post-mortem* analysis are encountered [2,5,6]. Although still underexploited compared to conventional materials characterization approaches, a few recent studies have demonstrated the potential of micro-XRF and micro-XANES in studying degradation phenomena, interfacial chemistry, and redox evolution in electrochemical systems such as solid oxide-based electrochemical cells. This emerging application highlights the promising potential of X-ray microanalysis to reveal spatially and chemically resolved insights into the aging mechanisms and functional behaviour of advanced energy materials [7–10].

X-ray microspectroscopy effectively combines XRF microanalysis with micro-XANES spectroscopy. Micro-XRF provides highly accurate elemental mapping from characteristic secondary X-ray emissions, making it ideal to identify interdiffusion zones, phase segregation, and compositional gradients across interfaces [1]. In parallel, micro-XANES provides chemical information, including oxidation states and coordination environments, through space-resolved absorption spectra around element-specific absorption edges. When combined, these two approaches allow for a detailed picture of material behaviour, especially at interfaces or in systems undergoing redox, thermochemical, or electrochemical transformations [2,5,6]. While these techniques are well established individually, their combined application to materials electrodes operating under realistic conditions remains largely unexplored. In particular, the use of synchrotron-based micro-XRF/micro-XANES to directly correlate local redox chemistry, cation migration, and interfacial stability in real systems represents a novel approach for this class of materials. Their application under *in situ* and *post-mortem* conditions further expands their value, enabling monitoring of material degradation, redox cycling, or interfacial reactions under realistic working environments. These capabilities are particularly relevant for the study of solid oxide-based electrochemical devices, like Solid Oxide Cells (SOCs), working in both electrolysis (SOECs) and fuel (SOFCs) mode, which gained growing attention as efficient and sustainable technologies for energy conversion and storage, hydrogen-based [5,11,12]. A key bottleneck in SOCs is represented by the oxygen electrodes. Classical materials used for this purpose, typically classified as perovskite-type oxides such as lanthanum strontium manganite (LSM), often exhibit high overpotentials and chemical reactivity when put in contact with the electrolyte, which limit the applicability of SOCs at intermediate temperatures (500–700 °C) [13].

To mitigate these issues, advanced SOCs architecture often incorporates a buffer layer made of doped ceria or similar materials, particularly indicated for the intermediate temperature devices [13]. However, the requirement of high content of critical raw elements in both the oxygen electrodes to enhance their electrochemical properties, raising concerns about cost and resource availability [14].

This scenario highlights the importance of exploring alternative electrode materials that are more compatible with electrolytes and better suited for long-term and intermediate temperature operation. In particular, analyzing the electrode–electrolyte interface after prolonged use is essential to assess its chemical composition and stability. At the same time, reducing the reliance on critical raw materials remains a strategic objective for the development of sustainable and scalable SOCs technologies.

Despite their potential, SOCs technologies, especially those employing intermediate temperature SOFCs (IT-SOFCs) configurations, remain susceptible to degradation mechanism, such as cation interdiffusion, phase instability, and surface segregation, particularly at elevated temperatures and prolonged operating times. These processes involve low concentration of the secondary phases and surface segregation formation, making their detection and understanding particularly challenging. In this regard, the application of micro-XRF and micro-XANES provides a unique opportunity to identify these degradation phenomena with high spatial resolution and chemical sensitivity, thereby guiding the rational design of durable, high-performance materials through a better fundamental understanding of chemical solid-solid processes [7,8,15,16].

Based on previous X-ray micro spectroscopy studies on the relative stability between cathode and electrolyte materials for SOFCs [11, 17–22], this work presents an integrated approach exploiting micro-XRF and micro-XANES for chemical and structural characterization of spent SOCs after electrochemical polarization in operating conditions. X-ray micro spectroscopy allows to investigate the possible interdiffusion that may occur at the electrode/electrolyte interface after the operation. Moreover, micro-XANES was carried out to acquire spectra on specific points to microscopically study the oxidation state and the chemistry at the Fe absorption K-edge along the interface as well as in the electrode bulk. This study highlights how these advanced techniques can contribute to unveil interfacial dynamics, compositional stability, and redox behaviour in realistic environments, ultimately contributing to the development of robust solid-state hydrogen technologies. Among the wide range of mixed ionic-electronic conductors investigated in the lasts years as electrode materials for SOCs, perovskite-type oxides based on $SrFeO_3$ have drawn increasing attention due to their high redox flexibility, relatively low cost, and earth-abundant composition [23–30]. Despite some well-documented challenges, including the segregation of Sr^{2+} at high temperatures, the formation of secondary phases at the electrode-electrolyte interface, and structural instability under redox cycling, this class of materials remains a promising alternative to more conventional perovskites such as LSCF and LSM [31–33]. Unlike cobalt or rare earth-rich compositions, $SrFeO_3$-based systems that rely on a lower content of critical raw materials, are more attractive for large-scale and long-term energy application [23]. In this work, we propose strategic doping with Ca, Ba, or Mo to improve phase stability, suppress Sr segregation, and tune the electrochemical performance, while maintaining the environmental advantage of reduced content of critical raw materials. Here, we discuss the structural and electrochemical behaviour of Ca-, Ba-, and Mo-doped $SrFeO_3$-based perovskites as potential electrode candidates for SOCs operation in intermediate temperature regimes, in contact with $Ce_{0.9}Gd_{0.1}O_2$, one of the most studied electrolytes for IT-SOCs devices [24,34]. We then partially substitute Sr with Ca and Ba with the aim of modulating the crystal structure, thermal expansion behaviour, and oxygen vacancy concentration, while Mo is introduced on the Fe-site to enhance redox stability and electronic conductivity [24,35,36]. The resulting multi-doped composition leads to a medium-entropy perovskite system, where the configurational entropy is expected to contribute to phase stability and redox properties improvement, with promising electrochemical performance under the redox conditions typical of IT-SOFCs and IT-SOECs

operation. Furthermore, with the aim of further reducing the amount of critical raw metals, a $CaFeO_3$, Sr- and Ba-doped system is here proposed and investigated to reduce the impact of Sr, however, this resulted in the formation of two distinct crystalline phases [37,38]. Overall, this study provides a comprehensive evaluation of how compositional tuning directly affects phase stability, ionic mobility, and interfacial reactivity. Among the investigated samples, the multi-doped composition with a higher content of Ca (10 wt%) exhibited the most balanced combination of structural robustness and electrochemical activity, confirming the suitability of the proposed doping strategy. The integrated analysis approach adopted offers valuable insights into the relationship between structure and function across the different samples, supporting the development of durable, resource-convenient electrode materials for next-generation solid oxide energy technologies.

2. Experimental section

2.1. Synthesis, characterization and methods

$Sr_{0.85}Ba_{0.075}Ca_{0.075}Fe_{0.80}Mo_{0.20}O_{3-\delta}$ **(SBCFM),** $Sr_{0.85}Ba_{0.05}Ca_{0.10}Fe_{0.80}Mo_{0.20}O_{3-\delta}$ **(SBC10FM)** and $Ca_{0.85}Ba_{0.05}Sr_{0.10}Fe_{0.80}Mo_{0.20}O_{3-\delta}$ **(CBSFM)** powders were prepared by solution combustion synthesis using $Sr(NO_3)_2$ (99.97%, Alfa Aesar), $Ba(NO_3)_2$ (99.95%, Alfa Aesar), $Ca(NO_3)_2 \cdot 4H_2O$ (99%, Sigma Aldrich), $Fe(NO_3)_3 \cdot 9H_2O$ (99%, Sigma Aldrich) and $(NH_4)_6Mo_7O_{24} \cdot 4H_2O$ (99%, Merck). Citric acid (>99.5%, Sigma Aldrich) was employed as a combustion fuel. The fuel-to-oxidizer ratio was set to 1 with NH_4NO_3 (99%, VWR), and the pH was set to 6 with NH_3 (25% solution, Sigma Aldrich). The solution was stirred at 150 rpm and 80 °C until combustion. The resulting powders were calcined at 1000 °C for 5h with a heating rate of 10 °C/min, and the resulting names and formulas are recapped in Table 1 [39,40]. $Ce_{0.9}Gd_{0.1}O_2$ **(GDC)** was used as received (Praxair, 99.9%).

The electrode powders were characterized by X-ray diffraction (XRD) using a Rigaku Miniflex 600 diffractometer in Bragg-Brentano geometry with Cu K_α radiation. Morphological analysis was performed using a Phenom 146 Rox benchtop scanning electron microscope (SEM). Phase composition and microstructure are shown in Fig. S1. Rietveld refinements, TGA, TPR, and N_2 adsorption on the perovskite powders, along with a representative durability test, were discussed elsewhere [21].

Electrochemical behavior of the investigated materials was assessed by evaluating their conductivity, derived from Arrhenius plots, and the overpotentials associated with oxygen reduction and evolution reactions. To perform these tests, specific cell architectures were assembled. Dense $Gd_{0.1}Ce_{0.9}O_{2-\delta}$ (GDC) ceramic supports were prepared and characterized using a benchmarked in-house procedure, resulting in flat and dense ceramic disks (98% of theoretical density) with a thickness of 250 μm and a diameter of 2 cm. These GDC disks served as electrolytes for testing the oxygen-electrode electrocatalysts developed in this study.

For each material, an ink was prepared using a commercial ink vehicle (MaTeck) and ethanol as solvent. The mixture was sonicated for 2 h and then sprayed onto both sides of the GDC electrolyte, forming asymmetric electrodes. The active area of the working electrode was defined by the spray-deposition mask and was 0.126 cm^2 (circular spot, 4 mm in diameter). All current densities reported in the I–V/overpotential plots were calculated by normalizing the measured current to this geometrical area. While the electrochemically active area may differ from the geometrical one due to electrode porosity and microstructure, the geometrical area is used here to ensure reproducible normalization and comparability across samples. The counter/sensing electrode (2 cm^2) was deposited with a significantly larger area than the working electrode to minimize its contribution to the measured polarization and ensure that the response is dominated by the working electrode. The reference electrode, placed on the same side as the working electrode, consisted of platinum applied using Pt paste (Engelhard) [23,41,42].

Table 1
List of samples and composition.

SBCFM	$Sr_{0.85}Ba_{0.075}Ca_{0.075}Fe_{0.8}Mo_{0.2}O_{3-\delta}$
SBC10FM	$Sr_{0.85}Ba_{0.05}Ca_{0.1}Fe_{0.8}Mo_{0.2}O_{3-\delta}$
CBSFM	$Ca_{0.85}Ba_{0.05}Sr_{0.1}Fe_{0.8}Mo_{0.2}O_{3-\delta}$
GDC	$Ce_{0.9}Gd_{0.1}O_2$

The assembled cells were calcined at 1100 °C for 2 h, with heating and cooling ramps of 2 °C/min. After calcination, the cells were ready for electrochemical testing. Experiments were conducted using a custom test bench (Greenlight Innovation), adapted for symmetrical cell configurations. The setup included opposing alumina tubes pressed against the cell with controlled force and equipped with internal current collectors. Thermiculite O-rings ensured gas sealing and electrical insulation.

Two thermocouples were positioned near each side of the cell to accurately monitor operating temperatures. Air was fed into both alumina tubes at a controlled flow rate of 200 cm^3/min, ensuring identical atmospheric conditions for the working, counter, and reference electrodes. Electrochemical measurements were performed in the temperature range of 300–900 °C and included Electrochemical Impedance Spectroscopy (EIS), measured at 0V and in the frequency range 1 mHz–1MHz and amplitude of ±10 mV, to derive Arrhenius plots from series resistance (Rs) data, as well as cyclic I–V scans (±1 V) to determine overpotentials for the investigated electrocatalysts.

The spent cells after electrochemical testing were embedded in epoxy resin, crosscut, and polished to expose the cathode/electrolyte interface. The micro-XRF maps and micro-XANES spectra were collected in fluorescence mode at the SXM-II endstation at the beamline ID21 of the European Synchrotron Radiation facility (ESRF, France), exploiting the Fe K-edge (7.12 keV) (see details in S.I.) [43] Data treatment, maps representation and concentration profiles were obtained using PyMca 5.6.7 [10]. The concentration profiles were derived from the elemental XRF maps by averaging and normalizing the XRF signal across the entire map width, in a direction perpendicular to the electrode–electrolyte interface, and a 2-point smoothing was applied in all plots. The position of the interface used as the origin of the x-axis in all concentration plots displayed following is chosen heuristically placing the zero in the middle of the interface region. The concentrations of cations are normalized to their average bulk value, to better appreciate their evolution at the interface. Large variance in the concentration profiles is due to the porous nature of the perovskite powders.

3. Results and discussion

The SEM images of the electrode powders (Fig. S1), as expected from the synthesis method employed, revealed that the powders exhibit a porous and fluffy morphology for all the three samples, showing a perforated texture. The XRD patterns and the main reference crystalline phases that match the experimental diffraction peaks (Fig. S1), demonstrate a satisfactory phase purity of the crystalline structure for the samples SBCFM and SBC10FM and the coexistence of two phases for sample CBSFM, brownmillerite $A_2Fe_2O_5$ (with A predominantly Ca) and scheelite $AMoO_4$ (with A predominantly Ba).

Fig. 1a–d presents the electrochemical measurements performed on the specimens investigated in this study. Fig. 1a shows the Arrhenius plot, derived from the series resistance (Rs) values obtained via Electrochemical Impedance Spectroscopy conducted at 0 V, as described in the Experimental section. In the adopted three-electrode configuration, Rs predominantly reflects the overall ohmic contribution of the cell assembly (electrolyte, contacts, and interfacial contributions under the given conditions) and is therefore used here as a comparative indicator across samples, rather than as the intrinsic bulk conductivity of the electrode material alone. The plot includes the results for all tested specimens, alongside the reference curve of GDC ($Ce_{0.9}Gd_{0.1}O_2$). All measurements were carried out in air, excluding any electronic leakage

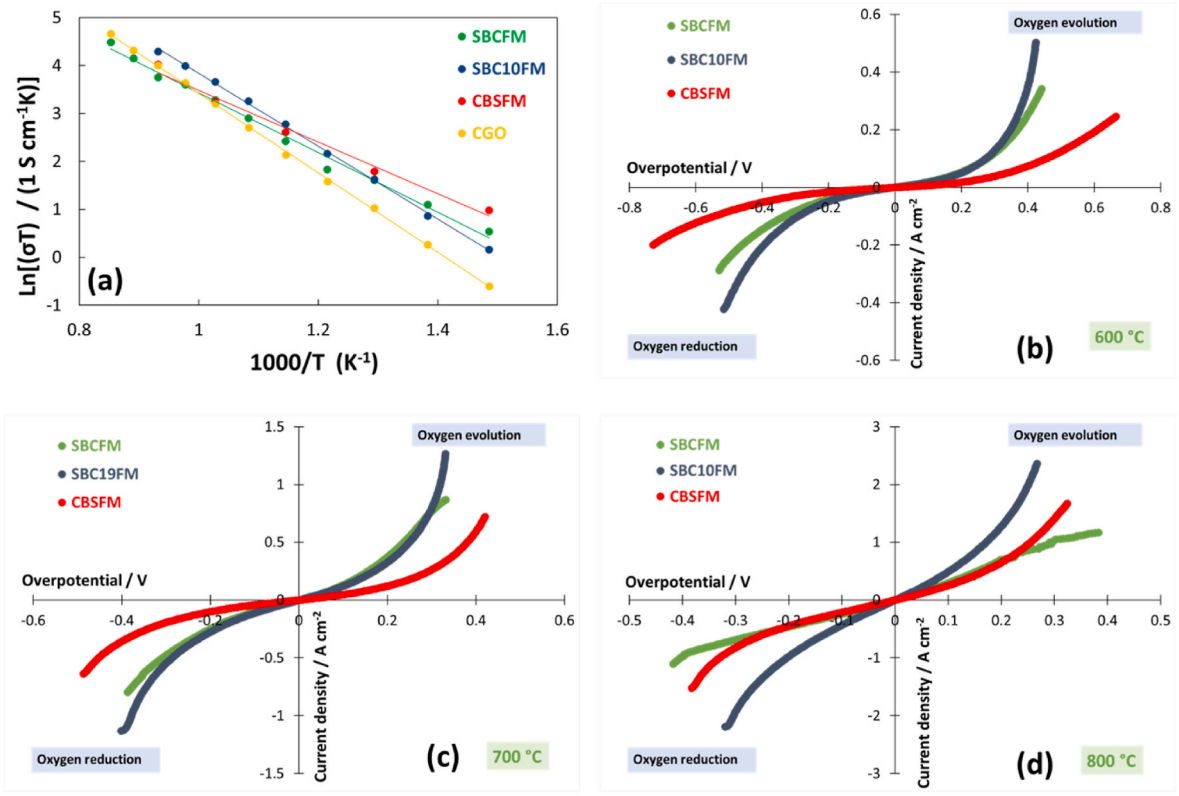

Fig. 1. Electrochemical characterization of SBCFM, SBC10FM and CBSFM electrodes on GDC. (a) Arrhenius-type plot of ln(σT) constructed from the high-frequency series resistance (Rs) obtained by EIS at 0 V (±10 mV) in air (σ calculated from Rs and the cell geometry; used here as a comparative indicator of the overall ohmic contribution of the cell assembly). (b–d) Overpotential (i–V) curves recorded between −1 and + 1 V at 600 °C (b), 700 °C (c) and 800 °C (d). Negative and positive current/potential quadrants correspond to ORR and OER, respectively.

effects that could arise from the presence of reducing agents. Compared to bare GDC, the presence of electrocatalyst layers can modify the apparent ohmic response of the assembly under small-signal excitation, consistent with facilitated oxygen exchange processes at/near the electrode–electrolyte interface.

At the lowest investigated temperature (400 °C), the CBSFM specimen, despite its low phase purity, showed the most favorable ohmic trend in the Arrhenius representation. However, this advantage diminished rapidly as the temperature increased. At intermediate and high temperatures, SBC10FM emerged as the best-performing material, while SBCFM showed marked deterioration, eventually becoming less performing than bare GDC.

The slopes of the Arrhenius curves provide insight into the apparent activation energy for oxygen ion migration, calculated using the Boltzmann equation. The activation energies were 0.71 eV for GDC, 0.54 eV for SBCFM, 0.65 eV for SBC10FM, and 0.47 eV for CBSFM. The low apparent activation energy of CBSFM is consistent with its composite (biphasic) nature, which may promote ion transport pathways at low temperature; however, this does not necessarily translate into superior electrode kinetics under polarization. In contrast, the rapid conductivity degradation in SBCFM may be attributed to phase de-mixing at elevated temperatures.

Fig. 1b–d shows the overpotential curves measured between −1 and + 1 V at 600 °C, 700 °C, and 800 °C, respectively. In this regime, performance is governed not only by ohmic contributions but also (and often predominantly) by polarization losses, including charge-transfer kinetics, effective mixed-conducting percolation, and the density/continuity of electrochemically active sites. At 600 °C and 700 °C (Fig. 1b–c), CBSFM, despite its favorable activation energy, performed worse than the other specimens, likely due to its biphasic nature. At 800 °C (Fig. 1a), SBCFM exhibited the poorest performance, consistent with its conductivity degradation and possible phase instability, while SBC10FM was the most efficient material, showing the highest activation energy and the most stable structural behavior.

Another important feature in Fig. 1b–d is the symmetry of the current–voltage curves. The negative quadrant corresponds to the oxygen reduction reaction (ORR), while the positive quadrant reflects the oxygen evolution reaction (OER). This dual behavior suggests potential applications of these materials as cathodes in SOFCs and anodes in SOECs. However, none of the specimens exhibited perfectly symmetrical behavior. All samples showed a more pronounced response in the OER region, particularly at lower temperatures.

The shape of the curves also provides insight into the dominant mechanisms. At low voltages and currents, the curves are primarily influenced by activation processes related to the formation of ionic oxygen species (ORR) and molecular oxygen (OER). At higher voltages and current densities, the response becomes increasingly ohmic-dominated; under the present test conditions, strong diffusion limitations are unlikely to dominate, although minor mass-transport effects cannot be fully excluded. The change in slope indicates a shift in the controlling mechanism.

Between 600 °C and 700 °C, SBCFM and SBC10FM exhibited similar activation constraints, but their performance differed due to their conductivity, as confirmed by the Arrhenius plot. In contrast, CBSFM showed limited electrocatalytic activity in this temperature range, affecting both ORR and OER.

At 800 °C, SBC10FM displayed minimal activation constraints, with performance increasingly influenced by ohmic and diffusion limitations, particularly above 1.7 A cm^{-2} in both quadrants. Conversely, SBCFM and CBSFM showed curves dominated by activation constraints up to 0.3 V. SBCFM also exhibited irregular behavior, likely due to degradation effects, while CBSFM showed a more regular curve shape, indicating

a transition to ohmic-dominated performance.

3.1. X-ray microspectroscopy

In all samples, the porous microstructure of the cathode layers, in contact with the dense electrolyte, is evident from XRF maps. This in turn is reflected in the concentration profiles, which appear uneven or flatter, respectively, in the cathode and electrolyte sides (Figs. 2–5). Moreover, it is very interesting to notice that Sr segregation was not detected in any sample after the electrochemical stress test, contrary to previous reports [31], proving that the strategic doping of $SrFeO_3$ with Ca, Ba and Mo may represent a promising approach to stabilize the electrode phase in contact with the electrolyte.

3.2. SBCFM/GDC

The XRF concentration maps of sample SBCFM/GDC and the corresponding profiles are reported in Fig. 2a, showing the distribution of the different cations at the interface.

A layer about 1 μm thick, enriched in Ca, Ba and Fe is evident at the interface. In this layer, the total fluorescence intensity is higher compared to the cathode, which indicates a net reduction in porosity. The extent of such accumulation is also visible in Fig. 2b, with the corresponding concentration profiles showing a relative maximum at the interface. We attribute the formation of this layer to the cell operation, as the highly porous electrode subjected to electrochemical polarization results in a densification in contact with the electrolyte. We also acknowledge that electronic transport in Fe-based perovskites can involve small-polaron hopping (Fe3+/Fe4+), and that polarization may locally modify oxygen chemical potential, potentially affecting polaron population and current distribution near the interface. However, the Fe K-edge micro-XANES collected across the interface does not show detectable changes in Fe edge features, indicating a stable mixed-valence state after operation. Therefore, within the sensitivity of our post-mortem analysis, the interfacial densification is more consistent with a confined, operation-induced microstructural/chemical redistribution (Ca/Ba/Fe enrichment) than with a pronounced polaron-driven redox shift at the interface. Moreover, it is worth noting that only some of the cations in the electrode are enriched in this densified zone (namely Ca, Ba and Fe) while the others (Sr and Mo) are not. This evidence suggests that the diffusion of the different cations of the electrode is driven by chemical or electrochemical effects rather than purely entropic mixing. The formation of this densification layer at the interface perfectly explains the electrochemical performances of SBCFM at 800 °C (Fig. 1d) that show a clear degradation effect of the electrode material. Since our microspectroscopy is post-mortem, we cannot extract growth kinetics from thickness–time data to rigorously distinguish active from passive regimes. However, the interfacial feature remains confined to ~1 μm and no extended interdiffusion into GDC is observed, suggesting a limited/self-limiting (passive-like) evolution rather than an actively growing reaction product. This interpretation is further supported by the Fe K-edge micro-XANES results discussed below, which show no appreciable changes in Fe coordination/oxidation state across the interface after polarization.

To further investigate any possible changes in the chemical state of iron at the interface after the electrochemical cycles, space-resolved Fe K-edge micro-XANES spectra were collected. The segregation of a divalent cation (e.g. Sr) in iron perovskite based electrodes with an A-

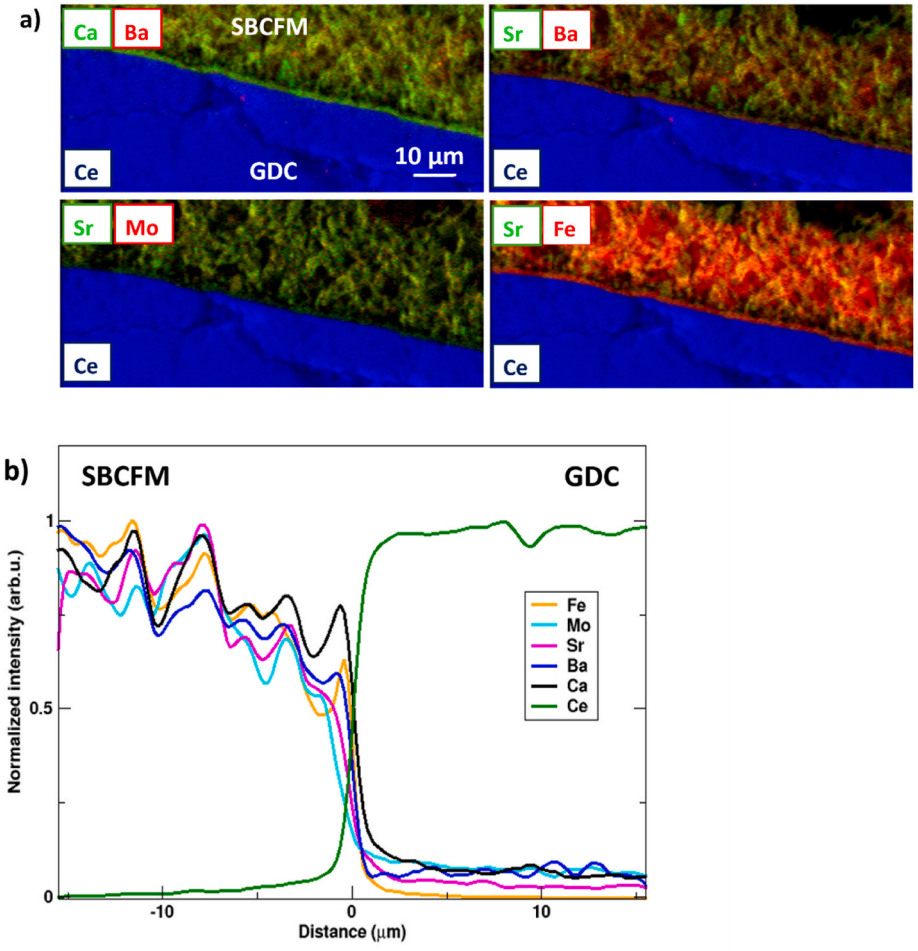

Fig. 2. a) Concentration maps of SBCFM/GDC from micro-XRF analysis. b) Concentration profiles of cations at the interface between electrode and electrolyte.

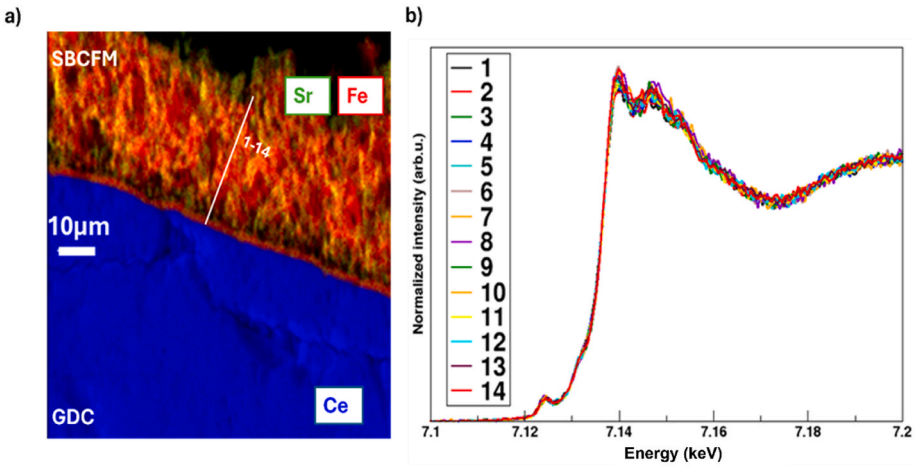

Fig. 3. a) XRF concentration map of Sr (green), Fe (red), and Ce (blue). The line shows the location of spots used to collect the Fe micro-XANES. b) Fe K-edge micro-XANES spectra collected at the different points. (For interpretation of the references to colour in this figure legend, the reader is referred to the Web version of this article.)

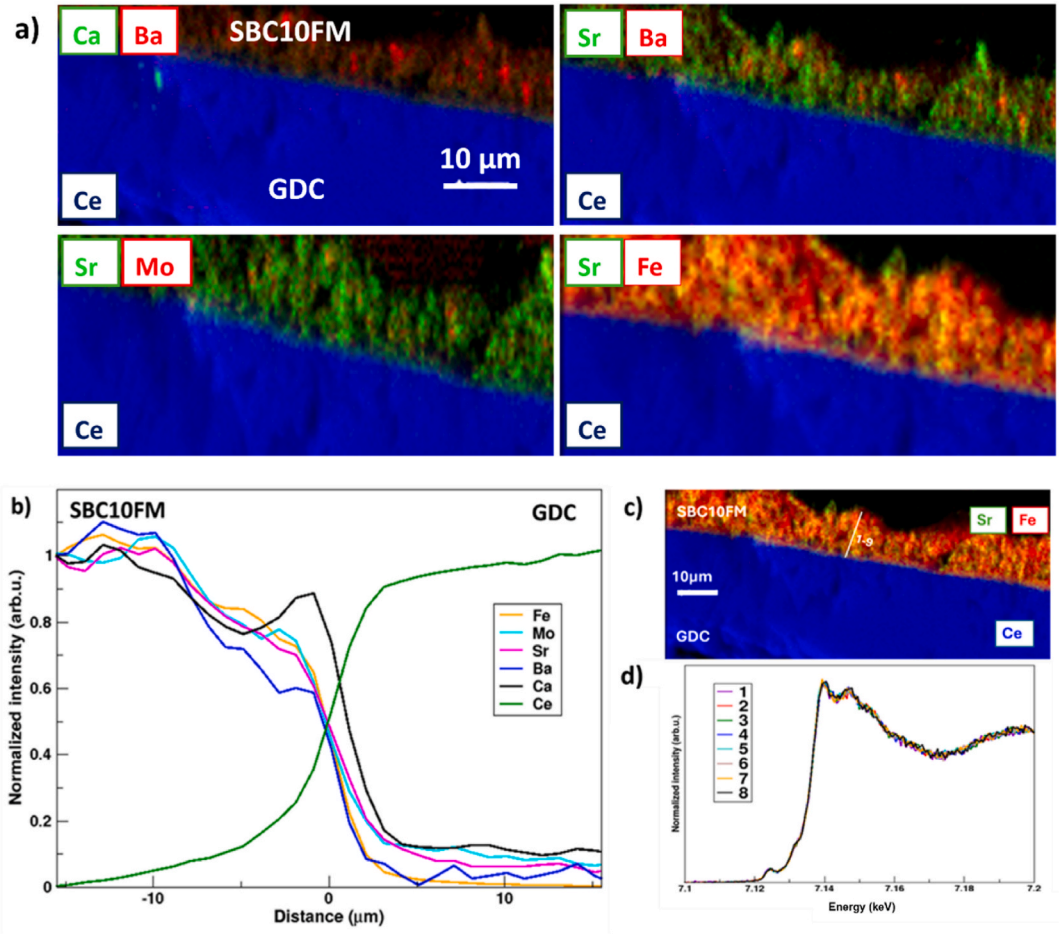

Fig. 4. a) Concentration maps of SBC10FM/GDC from micro-XRF analysis. b) Concentration profiles of cations at the interface between electrode and electrolyte. c) XRF concentration map of Sr (green), Fe (red), and Ce (blue). The line shows the location of spots used to collect the Fe micro-XANES. d) Fe K-edge micro-XANES spectra collected at the different points. (For interpretation of the references to colour in this figure legend, the reader is referred to the Web version of this article.)

site containing both divalent and trivalent cations, effectively reduced the average oxidation state of iron, in turn affecting the spectral features [44,45]. In Fig. 3b, the XANES spectra are reported over a perpendicular line probing different distances from the interface across the electrode, outlined onto the map in Fig. 3a.

The overall shape of the Fe absorption edge remains almost unchanged when moving across the interface towards the electrolyte. This suggests that the chemical environment, coordination geometry, and oxidation state of Fe (between +3 and + 4) is retained everywhere. As a further confirmation of the retention of Fe chemistry evaluated from the

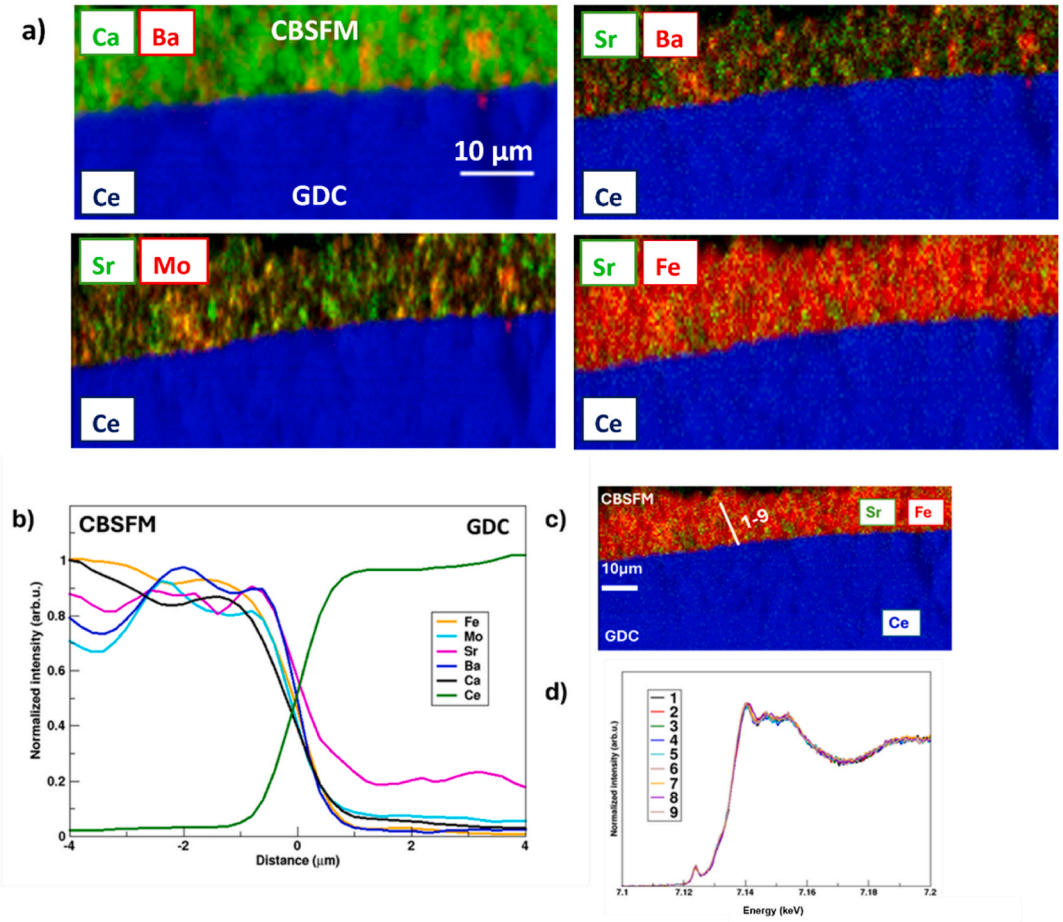

Fig. 5. a) Concentration maps of CBSFM/GDC from micro-XRF analysis. b) Concentration profiles of cations at the interface between electrode and electrolyte c) XRF concentration map of Sr (green), Fe (red), and Ce (blue). The line shows the location of spots used to collect the Fe micro-XANES. d) Fe K-edge micro-XANES spectra collected at the different points. (For interpretation of the references to colour in this figure legend, the reader is referred to the Web version of this article.)

micro-XANES we calculated the ratio between the intensity of the pre-edge peak and the main edge peak, plotted in Figure S9 a.

Based on this observation, some specific points were chosen to collect micro-XANES along the interface and in the electrode bulk phase, as further confirmation of no evident changes in the spectra. In Fig. S4, the XRF map and the average micro-XANES spectra are reported alongside the selected points in the electrode and interface regions and the interface points (white and red dashed dots, respectively).

This provides stronger evidence, averaged along the electrode and interface regions, that the chemical environment of Fe does not change because of electrochemical polarization, during the cell operation and despite the densification and relative increase in concentration of Ca, Ba and Fe at the interface, possibly forming an $AFeO_3$ phase (A = Ca,Ba). This observation, together with no evidence of Sr segregation and stability of Fe redox state, highlight the remarkable stability of the SBCFM phase in contact with ceria during operation.

3.3. SBC10FM/GDC

The micro-XRF maps, the concentration profile of SBC10FM/GDC sample and the micro-XANES spectra are reported in Fig. 4. No evident reaction features are detected at the interface, but in this case, however, no densification layer is visible at the interface, conversely to SBCFM/GDC (Fig. 4a). However, the concentration profiles (Fig. 4b) show that Ca does in fact accumulate at the interface close to the electrolyte. The interface diffusion zone here appears larger compared to SBCFM/GDC, due to higher cation mobility in the electrode phase, possibly driven by electrochemical polarization.

Such a striking difference in microstructural and chemical features at the interface (i.e. the absence of densification and the absence of Ba and Fe accumulation in SBC10FM) is determined by just a slight change in composition (on the order of 2.5% on A-site cations, cfr. Table 1). This suggests some kind of indirect stabilization of Fe in the crystal structure due to the higher amount of Ca and lower amount of Ba. At the same time, by increasing the concentration of Ca, it is possible to observe a higher migration rate of the Ca itself towards the electrode bulk, suggesting a significant lability of the cation in this phase.

The Fe K-edge micro-XANES spectra collected over a line of selected points (Fig. 4c), are reported in Fig. 4d. They are mainly unvaried and confirm that also for SBC10FM/GDC, iron retains its coordination and its pristine oxidation state (between +3 and + 4). The ratio between the pre-edge and the main peak is plotted in Fig. 9S b Based on these observations and considering also the overpotential characterizations (Fig. 1b–d), it is interesting to notice how the increase of the amount of Ca doping onto the A-site of the perovskite enhances the general phase stabilization. The iron chemistry is not affected, and the electrochemical performances of the SBC10FM/GDC are improved, suggesting a stabilization mechanism.

3.4. CBSFM/GDC

CBSFM composition, with Ca^{2+} as the main cation in the A-site, was chosen to investigate whether a reduction in the content of critical raw materials (Sr specifically) still leads to a single-phase perovskite, and to assess the impact of this modification on structural stability and electrochemical performance of the electrode. Although the resulting

sample is not single-phase, we proceeded with its characterization to evaluate how the presence of a secondary phase influences the overall properties.

The XRF maps, reported in Fig. 5a, show no evidence of reaction features, and no evident cation inhomogeneity at the micrometric scale, denoting a somewhat surprising and very interesting stability of the two-phase composite electrode. The concentration profiles in Fig. 5b confirm that there is no cation segregation at the interface. Compared to the other samples which have lower Ca content, the absence of Ca migration or accumulation of any kind is extremely interesting. These observations suggest that a higher Ca content in $SrFeO_3$-type perovskites does not affect the interaction stability between electrode and electrolyte.

The Fe K-edge micro-XANES spectra reported in Fig. 5d for this sample, across the interface (Fig. 5c) show no spectral changes, proving a remarkable stability of iron chemistry in the $Ca_2Fe_2O_5$ phase, retaining the same coordination and oxidation state, unvaried by the increased amount of Ca. Besides, the ratio between the pre-edge and the main peak is also plotted for this sample in Fig. S9c. We note that this pre-edge/main-edge metric is used here as a qualitative/semi-quantitative descriptor of local coordination asymmetry and defect-related distortion, rather than as a direct quantitative measure of oxygen non-stoichiometry (δ). Moreover, for oxygen electrodes operating under ORR/OER polarization, the oxygen content (and thus δ) can dynamically adjust with temperature, oxygen chemical potential and the applied electrochemical driving force; therefore, an ex situ "a priori" vacancy concentration would not necessarily represent the operando defect population relevant to performance. Despite its remarkable interfacial stability and favorable activation energy (Fig. 1a), CBSFM/GDC electrode performed electrochemically worse than the other samples at higher temperature, immediately visible from Fig. 1b–d, which is plausibly relatedto its biphasic nature and the resulting functional limitations (e.g., effective MIEC network/percolation and active-site density).

To better address the discussion about the coordination and the nature of the Fe chemistry in the studied samples, the XANES spectra of SBCFM, SBC10FM and CBSFM are reported in Fig. 6, together with the reference $SrFeO_3$ (SFO) and $LaFeO_3$ (LFO).

The Fe K-edge XANES spectra exhibit an intermediate line shape between Fe^{3+} and Fe^{4+} reference compounds, indicating a mixed or intermediate Fe oxidation state. Owing to the strong Fe–O covalency and electronic delocalization typical of Fe-based perovskites, as also widely reported in the literature [45]. In both SFO and LFO, Fe sits in a symmetrical octahedral coordination where, as widely discussed in the literature, the 1s → 3d transition is forbidden in the dipole approximation, which results in the flat pre-edge region of the spectra (7.12–7.13 keV) [46,47]. Doping ferrite perovskites as in our samples clearly induces an increase in the pre-edge peaks, indicating a removal of the perfect octahedral symmetry due to formation of vacancies and/or distortion of the FeO_6 octahedra. Such features, reflecting enhanced 3d–4p hybridization and relaxed dipole selection rules, are widely recognized in the literature as characteristic of doped Fe-based perovskites [48,49]. This observation further supports the electrochemical result since, for the best performing SBC10FM/GDC sample a higher catalytic active defect density is suggested by the enhanced catalytic performance. The CBSFM pre-edge is sharper compared to the other two samples due to the presence of FeO_4 tetrahedra in the brownmillerite structure, the introduction of vacancies or distortion for this sample does not compensate the electrochemical disruptive effect of the dual-phase nature, at higher temperature [46,47]. These observations confirm that the doping in all these cases brings about an important modification of the ideal octahedral coordination, and for the monophase sample, is directly related with the increased amount of oxygen vacancies, strategic defects for SOCs material [50].

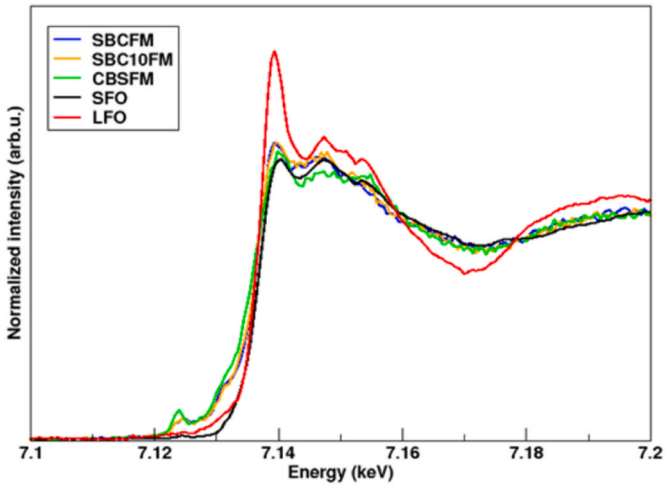

Fig. 6. Fe K-edge average micro-XANES spectra collected at the selected points of SBCFM (blue), SBC10FM (green), CBSFM (orange) and SFO (black) and LFO (red) as standards. (For interpretation of the references to colour in this figure legend, the reader is referred to the Web version of this article.)

4. Conclusions

Micro-XRF and micro-XANES, synchrotron light-based combined integrated approach, is exploited here for the chemical and structural characterization of SOCs after polarization under operating conditions. $SrFeO_3$-based perovskites co-doped with Ca, Ba, and Mo were investigated, selected for their high redox flexibility, low cost, and lower content of critical raw materials compared to conventional electrode materials. A key result is the absence of Sr segregation after electrochemical stress, that represents a classical degradation feature in the most common Sr-based electrodes exploited for SOCs materials. This finding confirms that the doping of $SrFeO_3$ with Ca, Ba, and Mo effectively stabilizes the electrode phase at the interface with the Gd-doped ceria electrolyte.

From an electrochemical perspective, the materials demonstrated a wide potential applicability both as cathodes for SOFCs and as anodes for SOECs. Among the tested compositions, SBC10FM emerged as the most efficient and high-performing material at intermediate-to-high temperatures, also exhibiting the greatest structural stability. The CBSFM sample, despite its biphasic nature, displayed a remarkable conductivity at lower temperature and the lowest activation energy for oxygen-ion migration (0.47 eV). This suggests that the coexistence of two homogeneously mixed phases may enhance ionic mobility.

Micro-spectroscopic investigations revealed distinct interfacial behaviors depending on the perovskite composition: for the SBCFM/GDC sample, a dense interfacial layer (~1 μm thick) enriched in Ca, Ba, and Fe was observed. This is attributed to chemical or electrochemical effects rather than simple entropic mixing, suggesting that cell operation promotes densification at the electrolyte interface.

On the other hand, in SBC10FM/GDC, a slight variation in Ca and Ba concentration does not give rise to a densification layer or accumulation of Ba or Fe. In fact, only Ca enrichment and migration toward the GDC were detected. Despite the microstructural changes, micro-XANES spectra revealed remarkable stability in the Fe chemistry across all samples. The Fe oxidation state (ranging between +3 and + 4) and its coordination environment were preserved both in the electrode bulk and at the interface, confirming the robustness of the multi-doped perovskite phases under electrochemical operation. XANES analysis also confirmed that doping induces distortion of the FeO_6 octahedra, evidenced by increased pre-edge peak intensity, which correlates with enhanced defect-related asymmetry and oxygen defectivity that can be beneficial for SOC performance, although this latter feature may change with temperature, oxygen chemical potential and electrochemical polarization (ORR/OER). The CBSFM composition specifically exhibited FeO_4

tetrahedra, characteristic of the brownmillerite structure, leading to a sharper pre-edge feature.

In conclusion, we demonstrate that $SrFeO_3$-based multi-doped perovskites, particularly SBC10FM, achieve an excellent balance between structural/interfacial stability (as shown by the suppression of Sr segregation and the chemical stability of Fe) and promising electrochemical performance. The combined use of micro-XRF and micro-XANES proves to be essential for unveiling incipient and punctual degradation mechanisms and guiding the rational design of durable, high-performance materials for solid oxide-based hydrogen technologies.

CRediT authorship contribution statement

Costanza Tedesco: Writing – review & editing, Writing – original draft, Formal analysis, Data curation. **Marta Ippolito:** Writing – review & editing, Writing – original draft, Data curation. **Marine Cotte:** Supervision, Software, Data curation. **Sebastian Vecino-Mantilla:** Writing – original draft, Data curation, Conceptualization. **Fabiana Matos de Oliveira:** Data curation, Conceptualization. **Massimiliano Lo Faro:** Writing – original draft, Supervision, Conceptualization. **Francesco Giannici:** Writing – original draft, Supervision.

Funding sources

This research was partially funded by the European Union - Next Generation EU (componente M4 C2, investimento 1.1) through grant PRIN 2022 PNRR “Oxygen electrodes for electrochemical Cells opErating at iNtermediate Temperatures without critical raw materials (OxCellenT)” prot. P20224RBBX, CUP B53D23027450001.

Declaration of competing interest

The authors declare that they have no known competing financial interests or personal relationships that could have appeared to influence the work reported in this paper.

Acknowledgements

We acknowledge the European Synchrotron Radiation Facility for provision of synchrotron radiation facilities under proposal number CH-6894 and we thank the staff of beamline ID21 for assistance and support. We thank the staff of Advanced Technologies Network (ATeN) Center, University of Palermo for assistance during the SEM measurements.

Appendix A. Supplementary data

Supplementary data to this article can be found online at https://doi.org/10.1016/j.jpowsour.2026.239536.

Data availability

The data that support the findings of this study are available from the corresponding author upon reasonable request. The raw data will be available at doi: 10.15151/ESRF-ES-2106988039 following a 3-year embargo.

References

[1] S. Bohic, A. Simionovici, X. Biquard, G. Martinez-Criado, J. Susini, Oil & Gas Science and Technology - Rev. IFP 60 (2005) 979.
[2] L. Mino, E. Borfecchia, J. Segura-Ruiz, C. Giannini, G. Martinez-Criado, C. Lamberti, Rev. Mod. Phys. 90 (2018) 025007.
[3] M. Cotte, K. Dollman, V. Fernandez, V. Gonzalez, F. Vanmeert, L. Monico, C. Dejoie, M. Burghammer, L. Huder, S. Fisher, W. De Nolf, I. Fazlic, H. Castillo-Michel, M. Salomé, M. Ghirardello, D. Comelli, O. Mathon, P. Tafforeau, Synchrotron Radiat. News 35 (2022) 3.
[4] A. Kostomitsopoulou Marketou, F. Giannici, S. Handberg, W. De Nolf, M. Cotte, F. Caruso, Anal. Chem. 93 (2021) 11557.
[5] B. Kaulich, P. Thibault, A. Gianoncelli, M. Kiskinova, J. Phys. Condens. Matter 23 (2011) 083002.
[6] X. Liu, W. Yang, Z. Liu, Adv. Mater. 26 (2014) 7710.
[7] L. Bernadet, J. Segura-Ruiz, L. Yedra, S. Estrade, F. Peiró, D. Montinaro, M. Torrell, A. Morata, A. Tarancón, J. Power Sources 555 (2023) 232400.
[8] F. Monaco, D. Ferreira-Sanchez, M. Hubert, B. Morel, D. Montinaro, D. Grolimund, J. Laurencin, Int. J. Hydrogen Energy 46 (2021) 31533.
[9] G. Martínez-Criado, J. Villanova, R. Tucoulou, D. Salomon, J.-P. Suuronen, S. Labouré, C. Guilloud, V. Valls, R. Barrett, E. Gagliardini, Y. Dabin, R. Baker, S. Bohic, C. Cohen, J. Morse, J. Synchrotron Radiat. 23 (2016) 344.
[10] V.A. Solé, E. Papillon, M. Cotte, Ph Walter, J. Susini, Spectrochim. Acta B Atom Spectrosc. 62 (2007) 63.
[11] A. Chiara, F. Giannici, C. Pipitone, A. Longo, C. Aliotta, M. Gambino, A. Martorana, ACS Appl. Mater. Interfaces 12 (2020) 55537.
[12] C. Su, W. Wang, M. Liu, M.O. Tadé, Z. Shao, Adv. Energy Mater. 5 (2015) 1500188.
[13] D. Montinaro, V. Sglavo, M. Bertoldi, T. Zandonella, A. Arico, M. Lofaro, V. Antonucci, Solid State Ionics 177 (2006) 2093.
[14] Study on the Critical Raw Materials for the EU 2023 – Final Report.
[15] J. Villanova, S. Schlabach, A. Brisse, A. Léon, J. Power Sources 421 (2019) 100.
[16] G. Sassone, O. Celikbilek, M. Hubert, K. Develos-Bagarinao, T. David, L. Guetaz, I. Martin, J. Villanova, A. Benayad, L. Rorato, J. Vulliet, B. Morel, A. Léon, J. Laurencin, J. Power Sources 605 (2024) 234541.
[17] F. Giannici, A. Chiara, G. Canu, A. Longo, A. Martorana, ACS Appl. Energy Mater. 2 (2019) 3204.
[18] F. Giannici, G. Canu, M. Gambino, A. Longo, M. Salomé, M. Viviani, A. Martorana, Chem. Mater. 27 (2015) 2763.
[19] F. Giannici, G. Canu, A. Chiara, M. Gambino, C. Aliotta, A. Longo, V. Buscaglia, A. Martorana, ACS Appl. Mater. Interfaces 9 (2017) 44466.
[20] A. Chiara, G. Raimondi, R. Merkle, J. Maier, C.V. Bordenca, C. Pipitone, A. Longo, F. Giannici, ACS Appl. Mater. Interfaces 15 (2023) 50225.
[21] G. Canu, F. Giannici, A. Chiara, G. Confalonieri, A. Longo, M.T. Buscaglia, M. Dapiaggi, V. Buscaglia, A. Martorana, J. Alloys Compd. 857 (2021) 157532.
[22] A. Chiara, G. Canu, A. Longo, C. Pipitone, A. Martorana, F. Giannici, Electrochim. Acta 401 (2022) 139495.
[23] F. Deganello, M. Ippolito, F. Giannici, C. Aliotta, L.F. Liotta, S. Vecino-Mantilla, Z. Hafsi, M. Lo Faro, Design of Multi-Doped Strontium Ferrate Perovskite-based Electrocatalysts with Medium-Entropy and Reduced Content of Critical Elements, Elsevier BV, 2025.
[24] Y. Li, N. Mushtaq, Y. Chen, W. Ye, Z. Zhuang, M. Singh, Y. Jing, L. Fan, Adv Funct Materials 35 (2025) 2411025.
[25] V. Zapata-Ramírez, G.C. Mather, M.T. Azcondo, U. Amador, D. Pérez-Coll, J. Power Sources 437 (2019) 226895.
[26] H. Ma, S. Li, S. An, M. Li, R. Sun, Q. Guo, ACS Omega 9 (2024) 24633.
[27] X. Dong, S. Yu, Y. Gu, L. Bi, Sustain. Mater. Technol. 41 (2024) e01104.
[28] G. Xiao, Q. Liu, S. Wang, V.G. Komvokis, M.D. Amiridis, A. Heyden, S. Ma, F. Chen, J. Power Sources 202 (2012) 63.
[29] S. Kumar, A. Das, S. Omar, ACS Appl. Energy Mater. 6 (2023) 2049.
[30] C. Yang, Y. Wang, Y. Tian, Z. Wang, J. Pu, F. Ciucci, B. Chi, Chem. Eng. J. 485 (2024) 149970.
[31] H.S. Slomski, J.L. Kaufman, M.J. Dzara, N.A. Strange, C. Priest, J.L. Hartvigsen, N. Kane, M. Casteel, B.C. Wood, D.S. Ginley, K.E. Kweon, B.P. Gorman, S. Shulda, ACS Phys. Chem. Au 5 (2025) 207.
[32] A. Beez, X. Yin, N.H. Menzler, R. Spatschek, M. Bram, J. Electrochem. Soc. 164 (2017) F3028.
[33] Y. Sun, S. He, M. Saunders, K. Chen, Z. Shao, S.P. Jiang, Int. J. Hydrogen Energy 46 (2021) 2606.
[34] P. Kaur, K. Singh, Sustain. Energy Fuels 9 (2025) 3981.
[35] M.M. Wu, Z. Li, L. Wen, S. Song, Y. Li, Y. Guo, X. Qiu, W. Wang, H. Zhang, Y. Liu, M. Wang, P. Han, Review of Materials Research 1 (2025) 100039.
[36] T. Jia, E.J. Popczun, J.W. Lekse, Y. Duan, Appl. Energy 281 (2021) 116040.
[37] X. Li, C. Shi, G. Zhang, G. Zheng, Z. Huang, X. Shen, J. Zhou, T. Chen, S. Wang, Ceram. Int. 49 (2023) 30187.
[38] L. Shen, Z. Du, Y. Zhang, X. Dong, H. Zhao, Appl. Catal. B Environ. 295 (2021) 120264.
[39] F. Deganello, A.K. Tyagi, Progress in Crystal Growth and Characterization of Materials, vol. 64, 2018, p. 23.
[40] F. Deganello, M. Ippolito, F. Giannici, C. Aliotta, L.F. Liotta, S. Vecino-Mantilla, Z. Hafsi, M. Lo Faro, Design of multi-doped strontium ferrate perovskite-based electrocatalysts with medium-entropy and reduced content of critical elements, Chem. Eng. J. 520 (2025) 165946.
[41] M.V. Barp, S. Vecino-Mantilla, F.M. De Oliveira, Z. Hafsi, L.G. Zandavalli, M. L. Faro, Electrochim. Acta 538 (2025) 146964.
[42] M.L. Tummino, L.F. Liotta, M. Lo Faro, S. Campagna Zignani, F. Deganello, J. Am. Ceram. Soc. 108 (2025) e20528.
[43] M. Cotte, E. Pouyet, M. Salomé, C. Rivard, W. De Nolf, H. Castillo-Michel, T. Fabris, L. Monico, K. Janssens, T. Wang, P. Sciau, L. Verger, L. Cormier, O. Dargaud, E. Brun, D. Bugnazet, B. Fayard, B. Hesse, A.E. Pradas Del Real, G. Veronesi, J. Langlois, N. Balcar, Y. Vandenberghe, V.A. Solé, J. Kieffer, R. Barrett, C. Cohen, C. Cornu, R. Baker, et al., J. Anal. At. Spectrom. 32 (2017) 477.

[44] J. Choi, D. Jang, M. Kim, J. Ha, H. Ahn, W.B. Kim, J. Mater. Chem. A 12 (2024) 12619.
[45] G. Raimondi, F. Giannici, A. Longo, R. Merkle, A. Chiara, M.F. Hoedl, A. Martorana, J. Maier, Chem. Mater. 32 (2020) 8502.
[46] E.R. Aluri, A.P. Grosvenor, J. Phys. Chem. Solid. 74 (2013) 830.
[47] M. Gyu Kim, H. Sang Cho, C. Hyun Yo, J. Phys. Chem. Solid. 59 (1998) 1369.
[48] T. E. Westre, P. Kennepohl, J. G. DeWitt, B. Hedman, K. O. Hodgson, E. I. Solomon, ..
[49] F. De Groot, Chem. Rev. 101 (2001) 1779.
[50] M. Christy, S. Choi, J. Kwon, J. Jeong, U. Paik, T. Song, Small Sci. 5 (2025).